

## Damage inhibition mechanisms in ultrasonic vibration-assisted scratching of monocrystalline silicon

Jing Zhao<sup>a</sup>, Quanli Zhang<sup>a,\*</sup>, Yan Chen<sup>a</sup>, Yandan Zhu<sup>b,\*\*</sup>, Chengqian Wang<sup>c,d</sup>, Zhimo Zhang<sup>c,d</sup>

<sup>a</sup> Jiangsu Key Laboratory of Precision and Micro-Manufacturing Technology, Nanjing University of Aeronautics and Astronautics, Nanjing, 210016, China

<sup>b</sup> Jiangsu Key Laboratory of Advanced Structural Materials and Application Technology, School of Materials Engineering, Nanjing Institute of Technology, Nanjing, 211167, China

<sup>c</sup> The 58th Research Institute of China Electronics Technology Group Corporation, Wuxi, 214000, China

<sup>d</sup> National Key Laboratory of Integrated Circuits and Microsystems, Wuxi, 214000, China

### ARTICLE INFO

**Keywords:**

Monocrystalline silicon  
Ultrasonic vibration-assisted scratching  
Ultrasonic overlap effect  
Subsurface damage

### ABSTRACT

Ultrasonic vibration-assisted grinding (UVAG) has made significant progress in improving the surface integrity of hard and brittle materials. However, the influence of ultrasonic overlap effect and ultrasonic motion trajectory on material removal mechanisms in monocrystalline silicon remains to be further understood, especially in micro-grinding of through-silicon vias (TSVs). In this work, the ultrasonic overlap effect and ultrasonic motion trajectory on the damage inhibition mechanisms during ultrasonic vibration-assisted scratching (UVAS) of monocrystalline silicon is investigated, combined with Smoothed Particle Hydrodynamics (SPH) simulation. The average error of the normal force and tangential force of UVAS between simulation and test is 10.6 % and 13.2 %, which verifies the validity of the scratch simulation model. Subsurface damage and stress field analysis reveal that a high ultrasonic overlapping rate results in significant interference and overlap of ultrasonic stress waves, effectively suppressing the propagation of median cracks and reducing the depth of subsurface damage. Additionally, the ultrasonic overlap effect suppresses the offset of the stress field at the vibration angle of 0, thereby reducing the length of lateral cracks and improving edge damage. The achieved results provide valuable insights into the ultrasonic vibration-assisted machining of hard and brittle materials and offer significant implications for the machining processes of micro-holes.

### 1. Introduction

Monocrystalline silicon is a widely utilized semiconductor material in large-scale integrated circuits (ICs), micro-electro-mechanical systems (MEMS), and medical implants, due to its excellent electrical and mechanical properties [1]. Through-silicon vias (TSVs) technology is particularly critical for enabling vertical interconnections in 3D ICs, effectively addressing the physical and economic limitations associated with traditional wiring methods, and enhancing the overall performance of semiconductor devices [2]. However, the high hardness and low fracture toughness of monocrystalline silicon present challenges in mechanical machining processes, often resulting in edge chipping, brittle fracture, and subsurface crack propagation [3]. These defects compromise the surface integrity and material strength of TSVs,

reducing the functional lifespan of 3D ICs. Ultrasonic vibration-assisted machining (UVAM) emerges as a versatile technology that allows efficient and cost-effective processing of materials, including silicon, glass, alumina, and composite materials [4]. Specifically, ultrasonic vibration-assisted grinding (UVAG), a hybrid technique combining UVAM with conventional grinding (CG), has demonstrated significant advantages in machining hard and brittle materials, including improved surface roughness [5], reduced grinding forces [6], minimized subsurface damage [7], and enhanced ductile material removal rates [8].

Recently, single abrasive grit scratching is widely applied to gain fundamental insights into the material removal mechanisms of hard and brittle materials [9], including the material removal morphology [10], ductile-to-brittle transition (DBT) depth [11], and subsurface crack propagation [12]. Liang et al. [13] and Zhang et al. [14] investigated the

\* Corresponding author.

\*\* Corresponding author.

E-mail addresses: [zhangql@nuaa.edu.cn](mailto:zhangql@nuaa.edu.cn) (Q. Zhang), [zhuyd@njit.edu.cn](mailto:zhuyd@njit.edu.cn) (Y. Zhu).

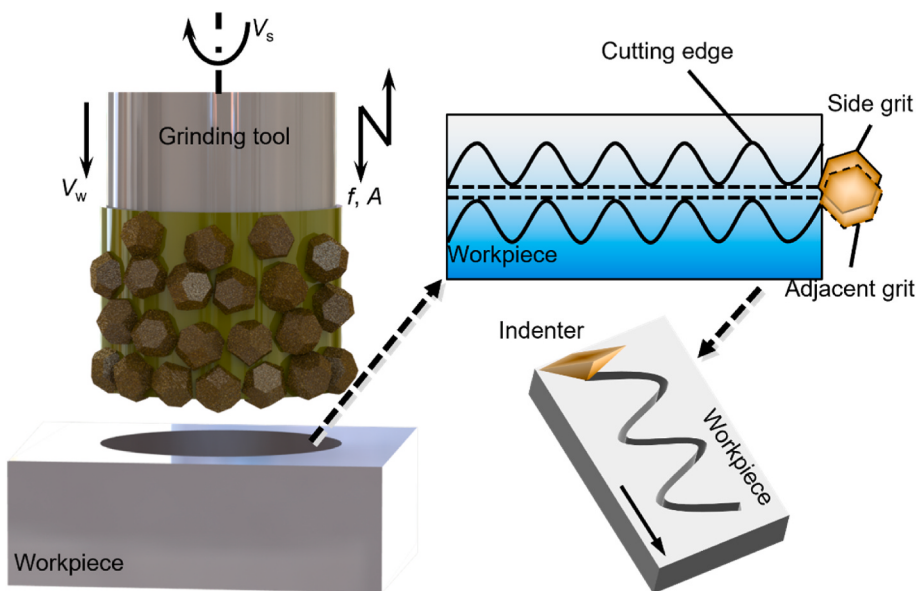


Fig. 1. Schematic diagram of the TSV abrasive grinding process.

removal mechanisms of C-plane sapphire by elliptical ultrasonic vibration and discontinuous ultrasonic vibration-assisted scratching (UVAS). The results revealed that ultrasonic vibration significantly reduced scratching forces and enhanced ductile material removal rate, while residual stress transitioned from tensile to compressive states with increasing scratch depth. Similarly, Sun et al. [15] performed continuous UVAS on Zerodur and ULE, showing that periodic variations in contact area and force between the indenter and the workpiece facilitated crack propagation in multiple directions, thereby improving material removal rates. Qiao et al. [16] explored UVAS of silicon nitride ceramics and found that material removal was dominated by deep lateral and radial crack interactions in conventional scratching (CS), while removal was principally driven by the intersection of shallow lateral cracks in UVAS. Most of these studies focused on exploring the effect of different processing methods and machining parameters on material removal, while the subsurface damage distribution characteristics of hard and brittle materials under ultrasonic effects need further exploration.

During machining, the stress state dynamically characterizes material deformation in real time. Numerical simulations can be employed to determine the stress field distribution of the workpiece subjected to the action of load, and the crack propagation process of the subsurface can be visualized. Currently, the most widely used numerical simulation methods to characterize the micro-cutting process include finite element method (FEM) [17], molecular dynamics (MD) [18], and smoothed particle hydrodynamics (SPH) [19]. The discrete particle model of SPH is of great advantage over other methods as far as the significant deformation, crack propagation, and the formation of discontinuous chips of brittle materials during machining are taken into consideration [20]. Li et al. [21] developed a coupled FEM-SPH model to analyze the scratching process of monocrystalline silicon with a Berkovich indenter and found that a smaller normal load could reduce subsurface damage, as well as the area and magnitude of the residual stress zone. Lin et al. [22] utilized the SPH method to simulate the scratching process of fused silica glass, revealing the mechanisms of crack initiation and propagation. Li et al. [23], by incorporating an SPH model for the scratching process on pre-stressed silicon, found that ductile mode grinding of monocrystalline silicon was more readily achieved under compressive stress conditions. Current SPH simulations have predominantly addressed CS processes, but the specific effects of continuous UVAS trajectories and overlap effects on crack evolution in monocrystalline silicon require systematic investigation.

In light of this, this work proposes a research framework to elucidate material deformation behaviors and damage mechanisms of monocrystalline silicon under ultrasonic effects. Through UVAS experiments, combined with surface topography characterization, subsurface microstructure analysis, and stress field distribution obtained from SPH simulations, we systematically reveal the material removal mechanism in UVAS. Particular emphasis is placed on investigating the effect of ultrasonic overlap effects and grit trajectories on macroscale surface damage behavior and microstructural evolution in monocrystalline silicon, providing a new perspective on the role of ultrasonic vibrations in damage inhibition in monocrystalline silicon.

## 2. Experiments and methods

### 2.1. Experimental methods of UVAS

The ultrasonic vibration applied to the sidewall grinding of TSVs was primarily continuous periodic contact and reciprocating polishing between abrasive grit and workpiece, the motion form is shown in Fig. 1. To simulate these vibration characteristics, UVAS tests were undertaken, as shown in Fig. 2b. In the experiment, a side-mounted Berkovich indenter (Taoxin Inc., China) was fixed to an ultrasonic vibration tool holder, and the geometry of indenter is shown in Fig. 2c. The workpiece was inclined at 0.573° and affixed to the side of a dynamometer to ensure parallel transmission of axial ultrasonic vibrations relative to the workpiece surface. Before the experiments, the frequency and amplitude of the indenter were measured by a laser Doppler vibrometer (OFV-5000, Polytec Inc., Germany). Detailed experimental parameters are shown in Table 1. The experiments were conducted under the temperature of (26 ± 1)°C and relative humidity of (45 ± 5)% RH.

The UVAS experiments of monocrystalline silicon were undertaken on the Sauer Ultrasonic 20 linear machining center (DMG MORI, Co., Ltd., Germany). The ultrasonic vibration system consists mainly of an ultrasonic power supply and an ultrasonic spindle. The power supply converts the industrial 50 Hz low-frequency current into high-frequency alternating current, while the piezoelectric transducer converts the high-frequency electrical signal into axial mechanical vibration. By turning on/off the ultrasonic vibration system, the machine can perform UVAS and CS operations. The commercially available (100) p-type monocrystalline silicon substrates (10 × 10 × 2 mm) (Powerwaywafer Inc., China) were selected as the workpiece. The as-received samples exhibited an initial surface roughness of less than 2 nm ( $S_a$ ). The

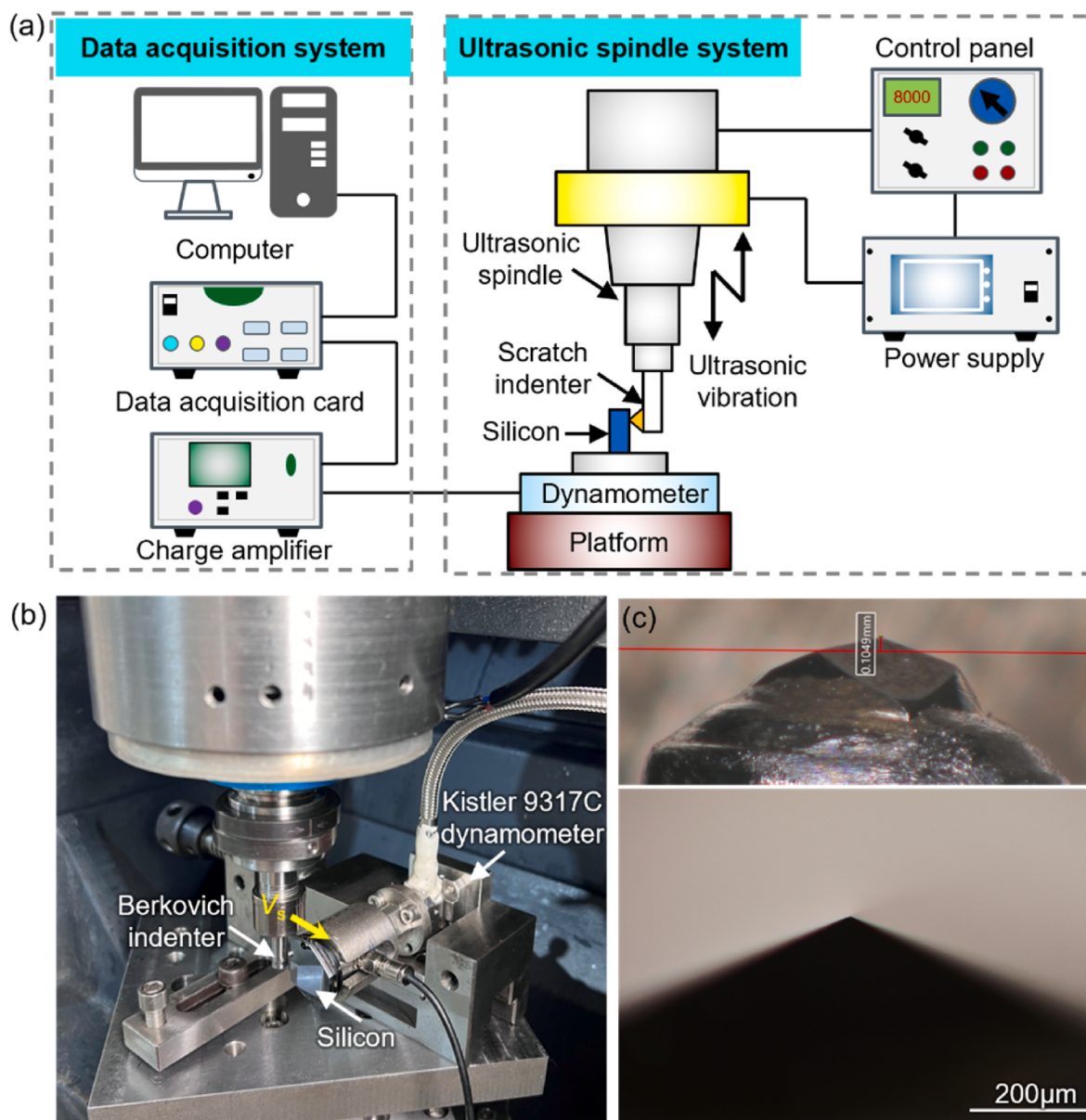


**Fig. 2.** Illustration of the experimental setup of UVAS: (a) Schematic diagram of ultrasonic equipment, (b) Installation diagram, and (c) Berkovich indenter image.

**Table 1**  
The specific parameters of the scratching experiments.

Parameter	Value
Ultrasonic parameters	
Frequency $f$ (kHz)	30
Amplitude $A$ ( $\mu\text{m}$ )	4
Scratching parameters	
Scratching speed (mm/min)	1, 5, 25, 125, 625
Scratching length (mm)	2
Depth of cut ( $\mu\text{m}$ )	0~20

monocrystalline silicon was bonded to a fixture using paraffin and fixed onto the dynamometers (9317C, Switzerland) by screws. The sampling frequencies of the dynamometers of 9317C were set to be 40 kHz. The electrical signals collected by the dynamometers were amplified by a charge amplifier and recorded on the data acquisition card. The measured force data were then saved and treated by the Dynoware software on the computer.

The surface morphologies of the scratched silicon were analyzed by a scanning electron microscope (EM-30PLUS, COXEM Co., Ltd., Spain).

Cross-sectional transmission electron microscopy samples, oriented perpendicular to the scratch direction, were prepared by a focused ion beam system (FEI-FIB Strata 400S, USA). Subsurface crack morphologies were subsequently examined with a field emission scanning electron microscope (Thermo Fisher Talos F200S/FEI Tecnai G2 F20 X-Twin, USA).

## 2.2. SPH simulation

### 2.2.1. Description of SPH method

Smoothed Particle Hydrodynamics (SPH) was first proposed by Gingold and Monaghan in 1977 as a grid-free Lagrangian method [24]. In SPH simulation, monocrystalline silicon is discretized into a set of arbitrarily distributed particles which maintain material properties and interact within a range described by the smooth kernel function. Transforming the conservation laws of continuum mechanics from differential to integral form yields the dynamic behavior of the entire system. The SPH method approximates the field variable function  $f(x)$  supporting any point in the  $\Omega$  field by a kernel function  $W(x - x', h)$  and

**Table 2**  
Monocrystalline silicon constants for the JH-2 constitution model.

Parameter	Density	Shear modulus	Intact normalized strength parameter	Fractured normalized strength parameter
Symbol	$\rho_0$	$G$	$A$	$B$
Unit	kg/m <sup>3</sup>	GPa	-	-
Value	2300	61.7	0.85	0.31
Parameter	Strength parameter for strain rate dependence	Maximum tensile strength	Maximum normalized fractured strength	Hugoniot elastic limit
Symbol	$C$	$T$	SFMAX	HEL
Unit	-	GPa	-	GPa
Value	0.013	0.26	0	9
Parameter	Parameter for plastic strain to fracture	Parameter for plastic strain to fracture	First pressure coefficient	Second pressure coefficient
Symbol	$D1$	$D2$	$K1$	$K2$
Unit	-	-	GPa	GPa
Value	0.02	1.85	201	260
Parameter	Elastic constants	Fracture strength parameter	Intact strength parameter	Failure criteria
Symbol	$K3$	$M$	$N$	FS
Unit	GPa	-	-	-
Value	0	0.21	0.29	0.024
Parameter	Pressure component at the Hugoniot elastic limit	Fraction of elastic energy loss converted to hydrostatic energy	Reference strain rate	
Symbol	PHEL	BETA	EPSI	
Unit	GPa	-	-	
Value	5	1	1	

realizes the continuum discrete into a series of particles with mass, stress-strain, velocity, and internal energy. The field variable function  $f(x)$  is expressed as:

$$\prod^h f(x) = \int_{\Omega} f(x') W(x - x', h) dx' \quad (1)$$

Where  $W$  is the kernel function,  $h$  is the smooth length of particles,  $x$  is the position vector of the arbitrary point,  $x'$  is the position vector of the approximate calculated point, and  $x-x'$  is the distance of particles.

The continuous matter is transformed into a discrete particle approximation, and the function value of the discrete point can be achieved by summing the values of the nearest adjacent particles, as

described by Eqn. (2). In the neighborhood of the interpolating core function, a variable of a certain particle  $i$  can be obtained by a weighted summation of particle set  $j$ ,

$$\prod^h f(x_i) = \sum_{j=1}^L \Psi_j f(x_j) W(x_i - x_j, h) \quad (2)$$

Where  $\Psi_j = m_j / \rho_j$  is the volume associated with particle  $j$ ,  $m_j$  and  $\rho_j$  ( $j = 1, 2, 3, \dots, L$ ) is the mass and density of particle set  $j$ , respectively.  $f(x_j)$  and  $L$  is the approximate function value of particle  $i$  and the total number of particles in the integral region, respectively.

### 2.2.2. Material constitutive model

Johnson-Holmquist model (JH-2) is applied for simulating the mechanical response and failure behavior under large deformation, high strain rates, and high pressure, which comprises a polynomial equation of states, a normalized smooth strength model considering both intact and fractured material and a damage model controlling the damage evolution of the elements [25]. To characterize the damage behavior of monocrystalline silicon during the UVAS process, the equivalent stress can be calculated as follows,

$$\sigma^* = \sigma_i^* - D(\sigma_i^* - \sigma_f^*) \quad (3)$$

Where  $\sigma_i^*$  is the normalized intact equivalent stress,  $\sigma_f^*$  is the normalized fracture equivalent stress.

The failure criterion of silicon is based on the damage degree  $D$ , which accumulates with the plastic strain, and it is expressed as Eqn. (4).

$$D = \sum \frac{\Delta \epsilon^p}{\epsilon_f^p}, 0 \leq D \leq 1 \quad (4)$$

Where  $\Delta \epsilon^p$  represents the equivalent plastic strain increment in each time step,  $\epsilon_f^p$  is the equivalent plastic strain of the material when brittle fracture occurs. In particular,  $D = 0$  and  $D = 1$  represents the intact and complete failure states of the material, respectively. Other simulation parameters for monocrystalline silicon are provided in Table 2. Additionally, the diamond grit possesses a density of 3.52 g/cm<sup>3</sup>, an elastic modulus is 1140 GPa, and a Poisson's ratio is 0.07.

Fig. 3 depicts the constitutive model for strength, damage, and fracture with element deletion capability under constant pressure and strain rate conditions. The effective plastic strain (EPS) fracture criterion triggers element removal once the equivalent plastic strain exceeds the critical failure strain (FS) threshold.

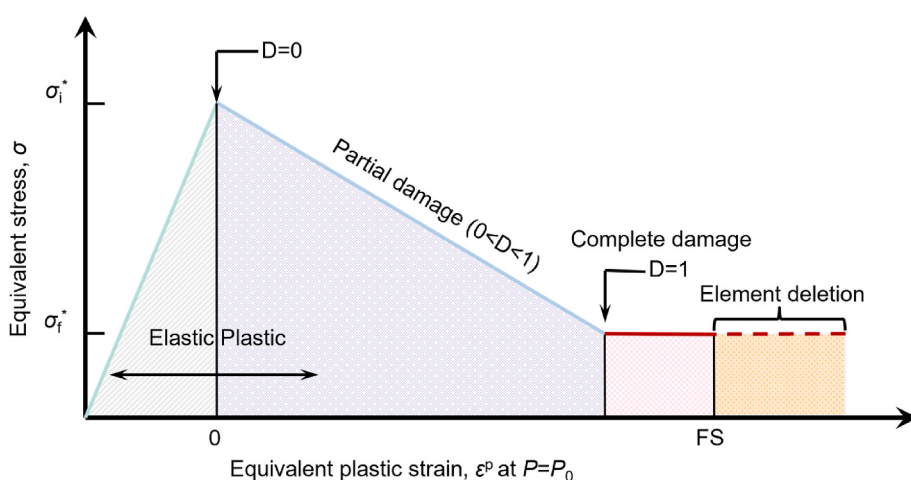


**Fig. 3.** Schematic diagram of damage failure in JH-2 constitution model.

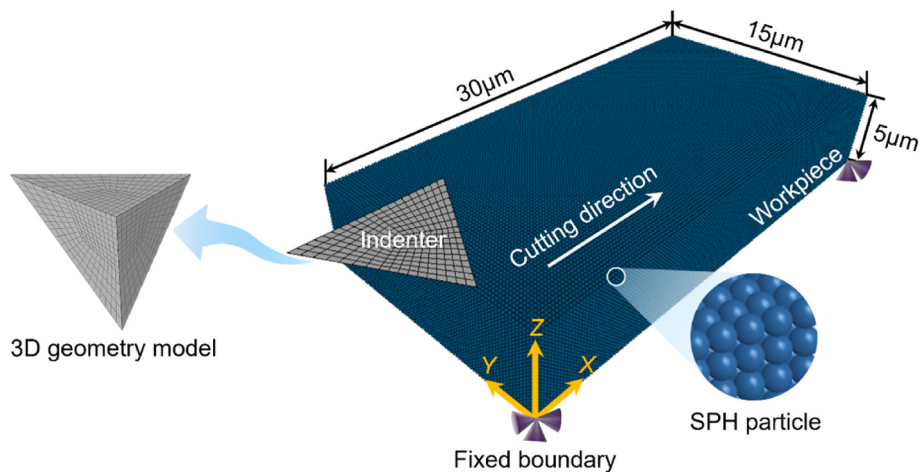


**Fig. 4.** The scratching simulation model in SPH.

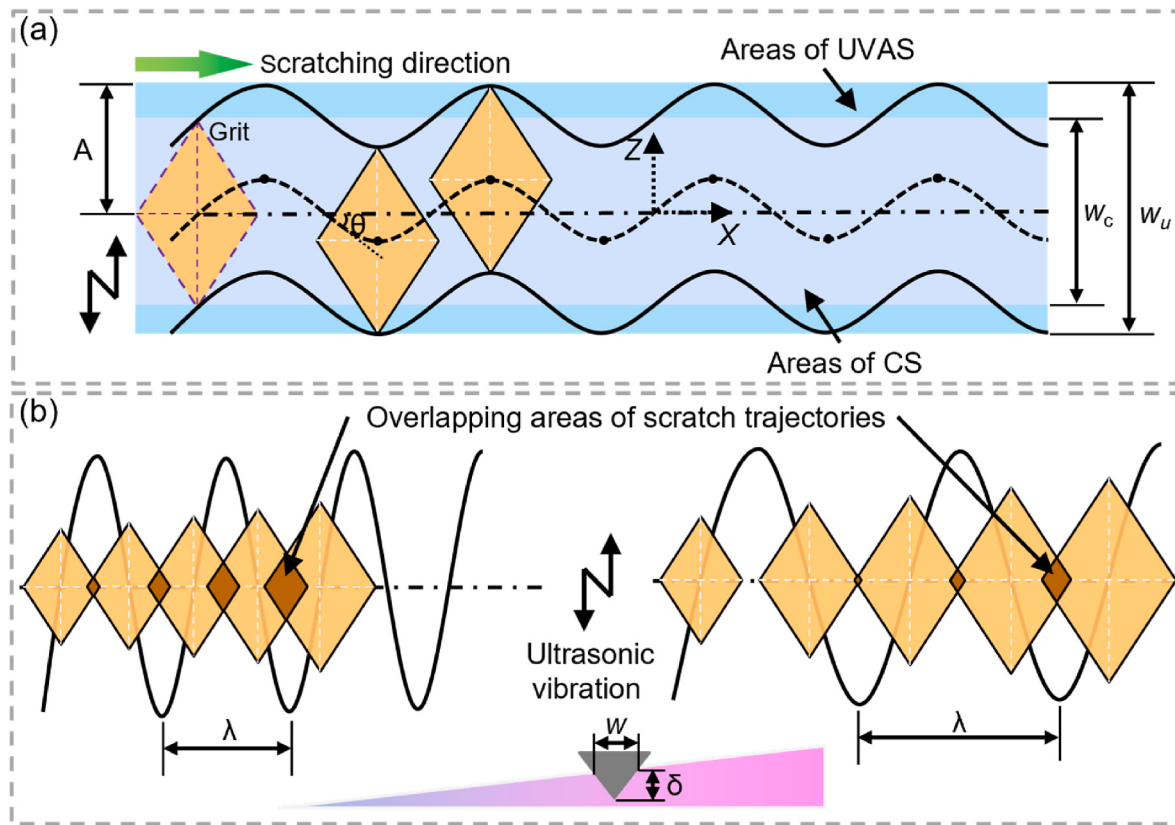


**Fig. 5.** Continuous scratching via ultrasonic reciprocation: (a) Indenter trajectory comparison between CS and UVAS, and (b) Overlap characteristics under varying vibration wavelengths in UVAS.

### 2.2.3. Simulation model

In the simulation, the workpiece is cubic with dimensions of 30  $\mu\text{m}$  (length)  $\times$  15  $\mu\text{m}$  (width)  $\times$  5  $\mu\text{m}$  (height), which consists of 283150 particles. A particle spacing of 100 nm was selected, below the critical DBT depth of silicon (approximately 158 nm [26]), to ensure plastic deformation characterization by at least one particle layer. The diamond Berkovich indenter is treated as an ideal rigid body and discretized using a finite element mesh. The distance between two particles of the workpiece is similar to the mesh size of the Berkovich indenter to prevent particle penetration [27]. The indenter is constrained except for the x- and y-movements in UVAS. All translations and rotations of the workpiece bottom are constrained, as shown in Fig. 4. In the simulation,

the diamond indenter traverses the cuboid workpiece from the left side to the right at a constant velocity of 1 mm/min and the simulation ultrasonic parameters are the same as the experiment.

## 3. Results and discussion

### 3.1. Evolution of material removal behaviors in UVAS at different overlapping rates

A series of UVAS experiments were conducted at the micron scale across varying scratching speeds. The indenter's motion trajectory in UVAS decomposes into two directions: (1) primary translation along the

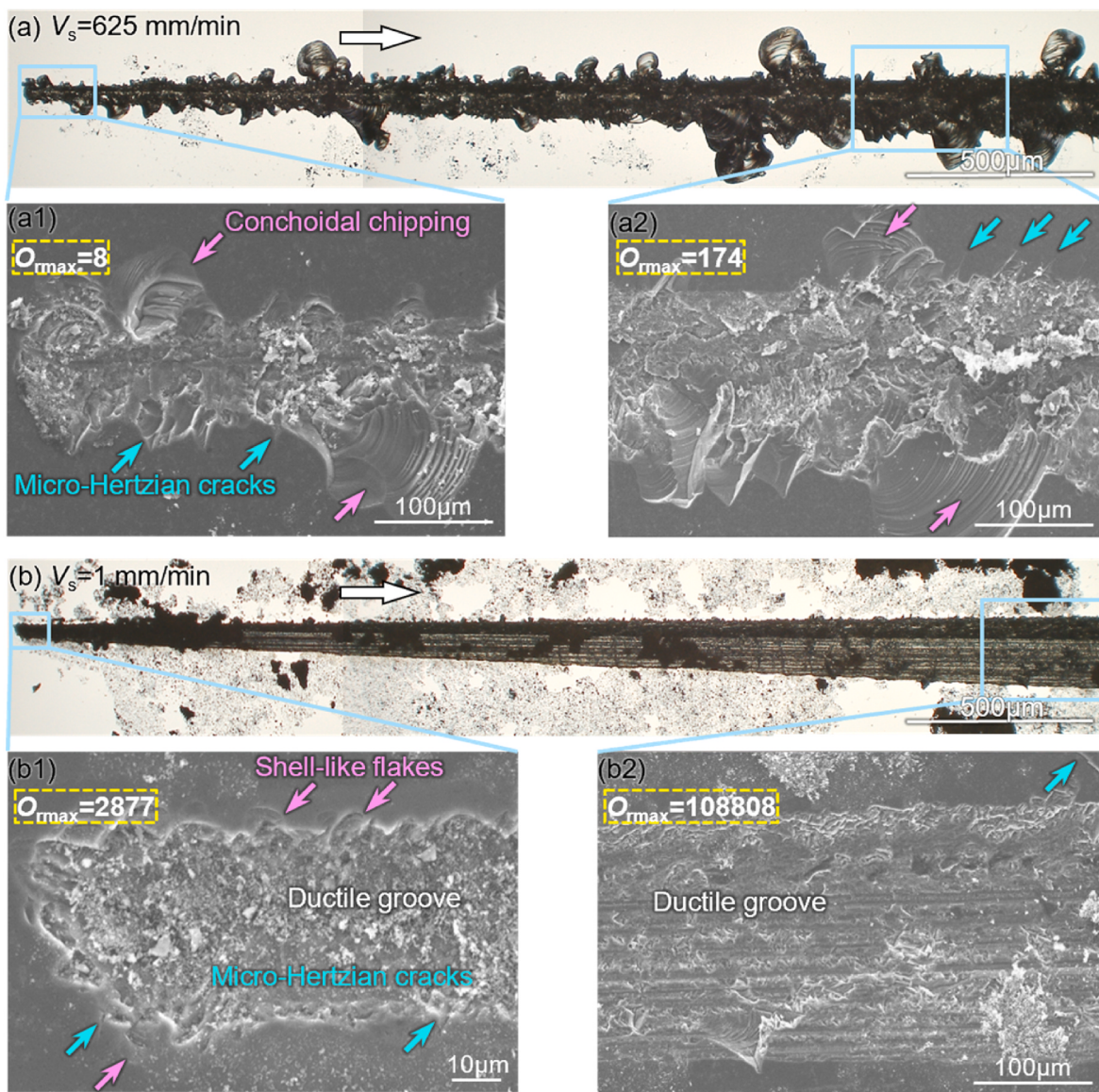


**Fig. 6.** Surface morphologies of scratch grooves in UVAS: (a1)  $O_{r\max} = 8$ , (a2)  $O_{r\max} = 174$ , (b1)  $O_{r\max} = 2877$ , and (b2)  $O_{r\max} = 108808$ .

scratching direction, and (2) reciprocating sinusoidal oscillation parallel to the workpiece surface. This ultrasonic vibration superimposes a sinusoidal trajectory onto the indenter's motion path, distinguishing UVAS from CS. Fig. 5a demonstrates that the scratch trajectory length in UVAS exceeds that of CS, with corresponding scratch widths satisfying  $W_u > W_c$ . To evaluate the reciprocating effect, the overlapping rate ( $O_r$ ) is defined as the number of repeated scratch passes per unit workpiece area during continuous scratching, expressed as [28]:

$$O_r = \frac{2w}{\lambda} - 1 \quad (5)$$

Where  $w$  is the cutting width of a single grit. The wavelength of the ultrasonic vibration curve ( $\lambda$ ) can be described by Equ. (6):

$$\lambda = \frac{v}{f} \quad (6)$$

Where  $v$  is the scratching speed.

Given that the cutting width of the diamond indenter ( $w$ ) is proportional to the penetration depth ( $\delta$ ) and the small size of the abrasive grits,  $\delta$  is approximated to be the same as  $w$ , as shown in Fig. 5b. In combination with Equs. (5) and (6), the relationship among the

overlapping rate ( $O_r$ ), vibration frequency ( $f$ ), scratching depth ( $\delta$ ), and speed ( $v$ ) is expressed as follows:

$$O_r = \frac{2\delta f}{v} - 1 \quad (7)$$

Where  $\delta$  is the penetration depth of the diamond indenter.

From Equ. (7), it can be seen that the overlapping rate decreases with the growing scratching speed, which indicates that the overlap and interaction between the ultrasonic vibration are weakened when the scratching speed increases. UVAS gradually transitions into CS when the speed is sufficiently high. Simultaneously, the overlapping rate exhibits a positive correlation with scratching depth, as shown in Fig. 5b.

Increased overlapping rates amplify reciprocation-induced polishing effects, fundamentally altering scratch topographies. Fig. 6 presents the residual surface topography of continuous UVAS with various depths under different scratching speeds, that is, under changed overlapping rates. The results in Fig. 6a indicate that when the maximum overlapping rate reaches 8 and 174, an increase in the number and size of Hertzian cracks on both sides of the scratch occurred, along with the formation of numerous cracks and brittle fractures within the groove. Additionally, a significant amount of large conchoidal chipping

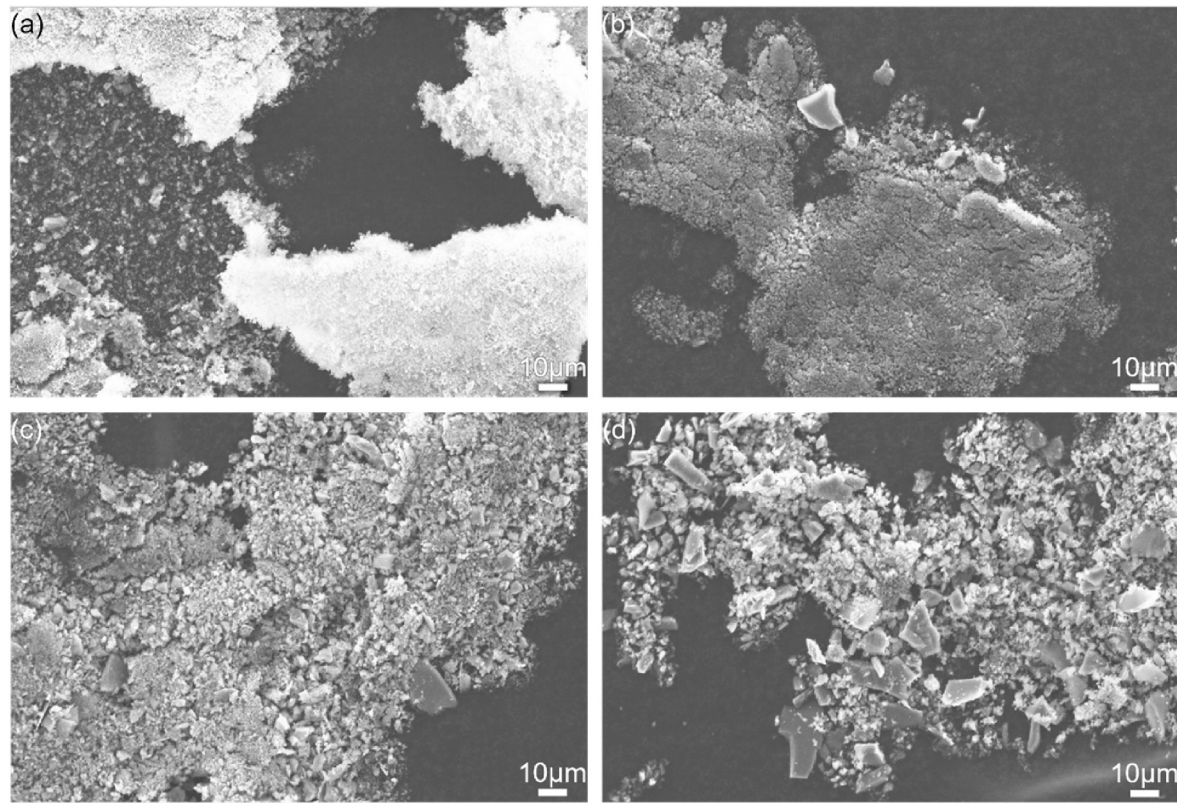


**Fig. 7.** Chip morphologies at different overlapping rates affected by the scratching speed: (a)  $v = 1$  mm/min, (b)  $v = 25$  mm/min, (c)  $v = 125$  mm/min, and (d)  $v = 625$  mm/min.

fractures formed at the scratch edges, with the overall process exhibiting distinct characteristics of brittle material removal. However, ductile grooves are present at the scratching speed of 1 mm/min, which suggests that different cutting mechanisms are involved in the material removal process at various overlapping rates. Small shell-like flakes and micro-Hertz cracks can be found at the scratch edges at the initial stage ( $O_{r\max} = 2877$ ), with fine chip debris covering the surface, as shown in Fig. 6b1. Although scratching depth increased to 20 μm under elevated overlapping rate conditions ( $O_{r\max} = 108808$ ), edge chipping is significantly suppressed, transitioning to predominantly smooth plastic edge morphology, as shown in Fig. 6b2.

Chip morphology analysis provides another critical insight into the material removal process and cutting modes under various overlapping rates, as shown in Fig. 7. In this study, chips were collected using adhesive conductive tapes and observed with SEM to investigate the chip formation mechanisms. At a scratching speed of 1 mm/min, chip formation experiences a layered morphology (see Fig. 7a), indicating the ductile-material removal mode. While the scratching macroscopically continued, the chips exhibit a loosely packed microstructure that confers considerable brittleness, causing immediate pulverization upon minimal contact. This structural behavior suggests that the cohesive force maintaining chip integrity does not originate from covalent bonds within the material but from significantly weaker interactions implying covalent bonds have been broken during processing. The findings further indicate that enhanced overlapping rates effectively suppress microcrack propagation, restricting the damage depth of the material to atomic dimensions. Conversely, at a 625 mm/min scratching speed, most chips fragmented into irregular particulate debris. The discontinuous lumpy chips exhibited distinct spallation features with submicron-scale acute edges (see Fig. 7d), indicating crack-propagation dominated formation mechanism under reduced overlapping rates.

### 3.2. Subsurface damages in UVAS at different overlapping rates

The cross-sectional morphology of the formed scratch at  $O_{r\max} = 8$  is shown in Fig. 8, where a sharp Berkovich indenter generates both lateral and median cracks within the subsurface material, exhibiting respective damage depths of 2.6 μm and 3 μm at the scratching depth of 300 nm. The interaction between Hertzian cracks and lateral cracking systems induces characteristic conchoidal spallation patterns along the groove edges. Additionally, interference between multiple median cracks appeared. Under  $O_{r\max} = 2877$ , cross-sectional images of monocrystalline silicon scratches (see Fig. 8c1) demonstrates multi-layered lateral cracking within near-surface regions, with the subsurface damage depths of 0.64 μm and 1.5 μm. Debris occurs when inclined micro-Hertzian cracks coalesce parallel lateral crack layers, inducing interfacial spallation. Median cracks are notably absent in these damage zones.

Cross-sectional TEM analysis of monocrystalline silicon grooves ( $O_{r\max} = 2877$ ) was conducted through FIB-fabricated lamellae to characterize atomic-scale subsurface damage mechanisms, as shown in Fig. 9. Before the ion beam processing, a platinum (Pt) protective layer was deposited to protect the structural integrity of the machined surface during sequential FIB milling and final thinning to electron transparency. Bright-field (BF) and dark-field (DF) TEM micrographs in Fig. 10a and b reveal the subsurface damage pattern of monocrystalline silicon, showing three typical structural regimes: I) a plastic deformation zone (PDZ) with 0.6 μm maximum thickness, II) a microcrack propagation zone containing lateral cracks, and III) the intact silicon matrix. The elevated overlapping rate induces substantial dislocation generation, resulting in increased dislocation density. Reduced dislocation slip distances inhibit sustained plastic deformation, promoting stress concentration and subsequent microcrack nucleation in silicon [7,29]. Consequently, the PDZ evolves into a hybrid fracture system consisting of lateral cracks, micro-Hertzian fractures, and microcracks. Microcrack accumulation facilitates energy dissipation and localized stress relief,

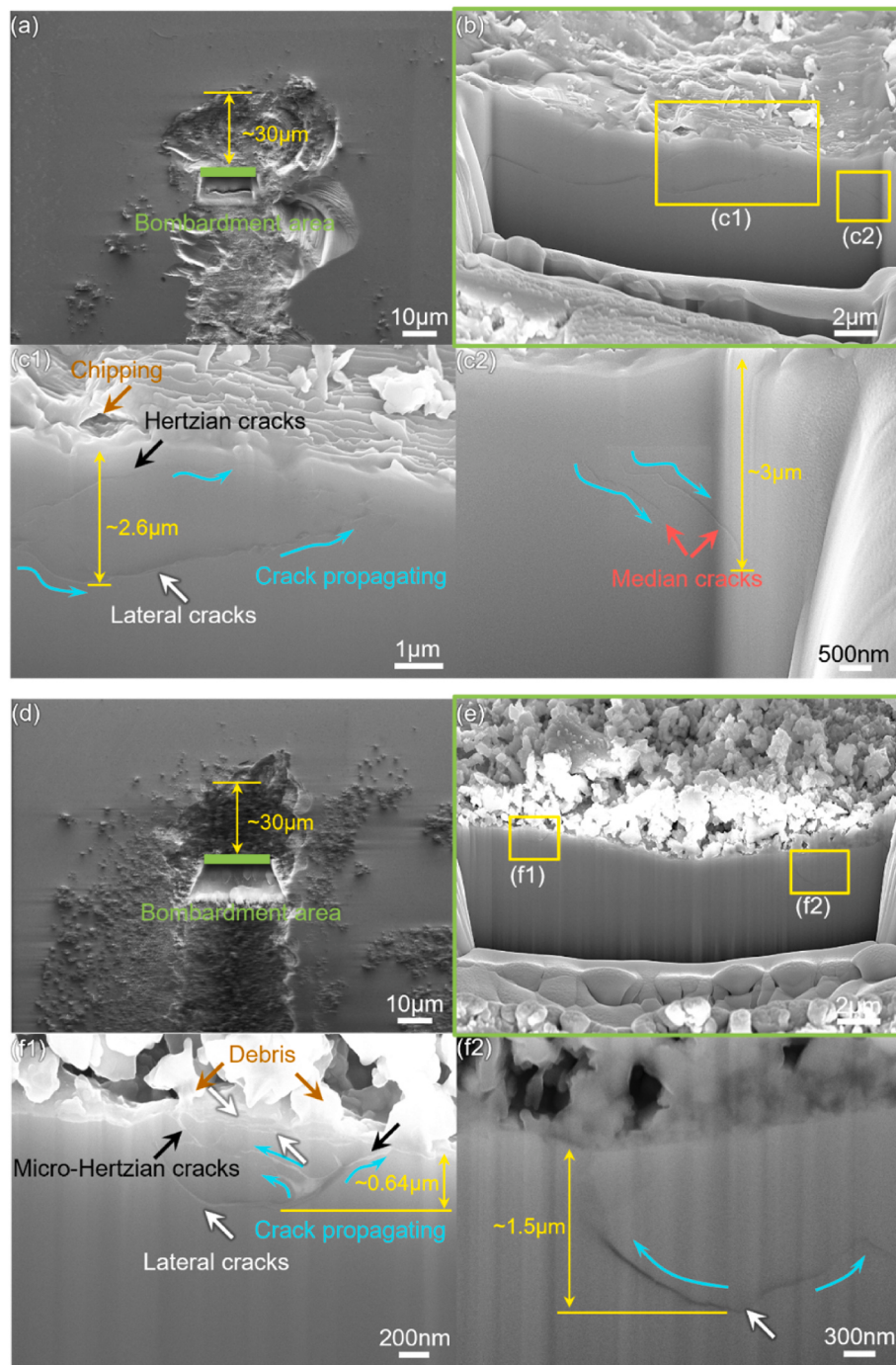


**Fig. 8.** (a) FIB extracted location at  $O_{r\max} = 8$ , (b) Subsurface cracking pattern at  $O_{r\max} = 8$ , (c1, c2) Locally enlarged view of the cracking pattern, (d) FIB extracted location at  $O_{r\max} = 2877$ , (e) Subsurface cracking pattern at  $O_{r\max} = 2877$ , (f1, f2) Locally enlarged view of the cracking pattern.

thereby suppressing macroscopic crack formation while enhancing material brittleness. The propagating lateral cracks exhibit horizontal interpenetration and coalescence, creating a self-delimited fracture zone that significantly impedes crack propagation into deeper subsurface domains of monocrystalline silicon. Region III retains the monocrystalline silicon structure with a few crystal plane slips, as shown in Fig. 10d. High overlapping rates induce crystal plane slip in multiple directions simultaneously, preventing the development of extended slips in any direction, thereby effectively reducing the subsurface damage depth in monocrystalline silicon scratches [30]. High-angle annular dark field (HAADF) image shows that Si and O are evenly distributed, which indicates that there are no other forms of crystalline structure

generated during the ultrasonic scratch process (see Fig. 10e and f).

Bright-field images of the powder-like chips are shown in Fig. 11a. Fig. 11b shows the high-resolution TEM (HRTEM) images of local regions selected from Fig. 11a. The HRTEM image of the powder-like chips shows the presence of incompletely amorphous ones containing a few crystallites. Furthermore, grain boundaries are observed between the crystallites, which indicates that, under the compressive stress exerted by the indenter, monocrystalline silicon transforms into nanocrystalline and amorphous phases. This also shows that the formation mechanism of powder-like chips is phase transformation and cleavage under the ultrasonic overlap effect [31].

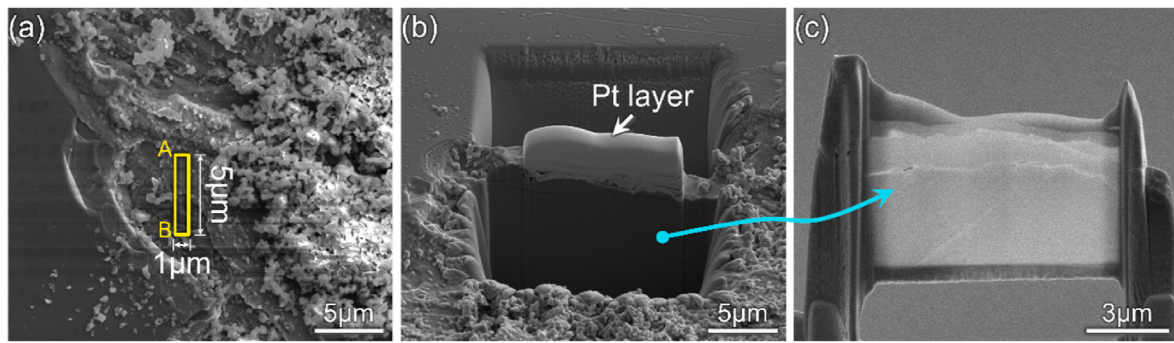


**Fig. 9.** TEM sample preparation: (a) FIB extracted location, (b) Sample morphology after being cut by FIB, and (c) FIB-thinned TEM sample.

### 3.3. Stress distribution in UVAS at different overlapping rates

To strengthen the validity of conclusions, SPH simulations provide complementary validation for experimental findings and deliver comprehensive mechanistic insights. Fig. 12 indicates the comparison results of simulated and experimentally measured forces, in which case  $F_x$  is the tangential force, and  $F_z$  is the normal force. The average error of  $F_z$  and  $F_x$  in simulation and scratching test is 10.6 % and 13.2 %, which verifies the validity of the scratch simulation model. The trends of the  $F_x$  and  $F_z$  curves obtained from both experiments and simulations are consistent with an upward inclination, and the amplitude of each force is close. In addition, Fig. 12 further demonstrates that material removal modes transfer synchronously from ductile removal (DR) and DBT to brittle removal (BR) in both experimental and simulated results. During the initial scratching stage,  $F_x$  and  $F_z$  exhibit a smooth increase, resulting from particle vibrations confined near initial positions without significant displacement. At  $t = 0.107$  s, simulated force curves exhibit pronounced fluctuations, indicating particle displacement beyond initial positions and subsequent microcrack initiation in the workpiece. However, the experimental values are lower than the simulation in the middle section of the curves, and the fluctuation of the experimental curves is significantly greater than that of the simulations. This discrepancy can be attributed to the presence of unpredictable material defects and vibrations during the machining process.

Fig. 13a1-c1 presents the crack distribution patterns under varying ultrasonic overlapping rates (quantified by wavelength  $\lambda$ ), with red damage particles indicating cracks. Significant conchoidal fracture features and Hertzian crack systems develop when the wavelength is  $\lambda$ , resulting in prominent brittle fracture material removal (see Fig. 13a1). In particular, the wavelength reduction to be  $\lambda/4$  induces the morphological transition of edge damage from macro-scale conchoidal fragments to shell-like flakes, showing a strong correlation with experimental observations. The crack initiation is dependent on the maximum principal stress, while the direction of crack propagation is influenced by the gradient tensile stress variation [27]. Fig. 13a2-c2 shows the principal tensile stress contour maps in the  $XOY$  plane under different ultrasonic overlapping rates, with black-dashed arrows indicating the crack propagation directions. The influence of ultrasonic vibration on the high tensile stress region results in a deflection effect, which significantly activates the crack nucleation zone (indicated by yellow arrows), thereby promoting the formation of Hertzian cracks at the scratch edges [32]. The size of the crack nucleation zone diminishes at a wavelength of  $\lambda/4$ , correlating with a marked reduction in the dimensions of the Hertzian cracks, which implies that an increased overlap in the ultrasonic trajectory can effectively reduce surface cracking during the grinding process. Furthermore, due to the deflection of the stress field along the grit motion direction, an additional small high-stress region was generated inward along the ultrasonic motion trajectory. That is, except the crack propagation tendency at the scratch edge, a potential crack growth region appeared within the ultrasonic

trajectory, as indicated by the yellow dashed circle. The interaction between surface cracks becomes more pronounced when the overlapping rate of the grinding tracks increases, leading to the formation of a fine debris layer on the grinding surface.

Fig. 14a1-c1 demonstrates that the maximum subsurface crack depth decreases from  $2.387 \mu\text{m}$  to  $1.757 \mu\text{m}$  when the wavelength decreases from  $\lambda$  to  $\lambda/4$ , resulting in a reduction of approximately 26.4 %. Numerous long median cracks form in the subsurface at the wavelength of  $\lambda$ , with observable interference between cracks, which is consistent with the subsurface crack distribution in Section 3.2. However, median cracks disappear when the wavelength reduces to  $\lambda/4$ , and only shorter Hertzian cracks remain. This transition resulted from the enhanced ultrasonic trajectory overlap effect leads to stress waves to propagate and superimpose, eventually promoting lateral propagation of tensile stresses beneath the plastic zone, as marked by yellow gradient arrows in Fig. 14c2. The shielding effect from these subsurface-parallel stress waves inhibits the propagation of median cracks into deeper layers of the material, causing the shorter cracks to concentrate near the surface. This suggests that the material exhibits enhanced resistance to crack propagation under high ultrasonic overlapping rates.

In analyzing the ultrasonic motion trajectories, the vibration amplitude ( $A$ ), vibration frequency ( $f$ ), and speed ( $v$ ) are the key influencing factors. To comprehensively describe the combined effects of these parameters, the term of the vibration angle is introduced. The vibration angle, denoted as  $\theta$ , is the instantaneous angle between the UVAS vector and feed direction. The vibration angle changes dynamically during the reciprocating motion of the indenter, as shown in Fig. 5a. In the coordinate , the corresponding scratching trajectory equation can be derived as:

$$z = A \sin\left(\frac{2\pi f}{v}x\right) \quad (8)$$

Where  $x$  represents the scratch length.

Thus, the vibration angle can be achieved as follows:

$$\theta = \arctan(z') = \arctan\left(\frac{2\pi Af}{v} \cos\left(\frac{2\pi f}{v}x\right)\right) \quad (9)$$

The monocrystalline silicon undergoes both indentation and shear effects induced by the abrasive grits in localized regions when the vibration angle dynamically varies within a single vibration cycle. The vibration angle is 0 when the indenter reaches the peak amplitude. To investigate the ultrasonic trajectory on crack initiation and propagation mechanisms, micro-segments at the vibration angle of 0 were compared at different ultrasonic wavelengths. The stress field distributions for each segment were sequentially presented as cloud maps, based on the order in which the abrasive grits passed through the cross-sections of the sine trajectory with a vibration angle of 0, as shown in Fig. 15. The white vertical dashed line in the figure denotes the position of the symmetry axis of the plastic zone located at the base of the indenter tip. It is found that the stress field around the scratch is offset to varying extents. The

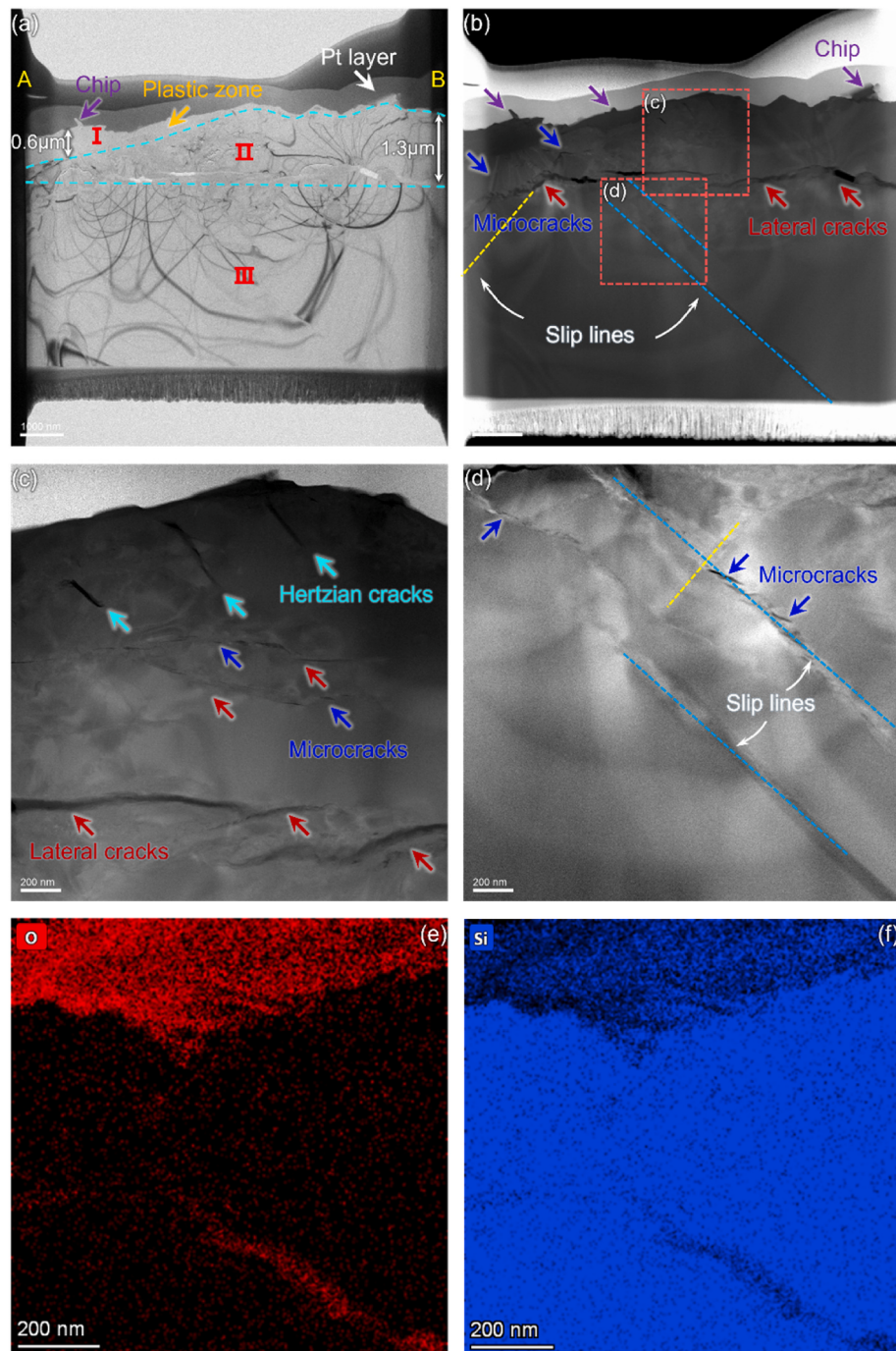


**Fig. 10.** Subsurface damage morphology of UVAS: (a) BF image, (b) DF image, (c, d) Locally enlarged view of the subsurface damage zone, and (e, f) HAADF image.

instantaneous stress field at each cross-section generates significant field distortion around the scratch at the wavelength of  $\lambda$ . The high tensile stress region at the upper vertex of the sine trajectory shifts to the left of the scratch, as shown in Fig. 15a1-c1. Similarly, the high tensile stress region at the lower vertex shifts noticeably to the right of the scratch, as shown in Fig. 15d1-f1. When the tensile stress exceeds the fracture strength of silicon, large conchoidal chipping occurs on both sides of the scratch edge, leading to brittle material removal. However, the instantaneous stress field at each cross-section becomes more uniform around the scratch at the wavelength of  $\lambda/4$ , and the stress field around the scratch is nearly symmetric, as demonstrated in Fig. 15a2-f2. The high tensile stress regions expand slightly on both sides of the scratch and reduce the length of lateral cracks. This results in the lateral cracks

propagating horizontally along both sides of the plastic zone, with only microcracks and micro-chipping appearing at the scratch edges. This is consistent with the damage distribution in the experiment, verifying the reliability of the JH-2 constitutive model.

### 3.4. Damage inhibition mechanism of high overlapping rate in UVAS

The high overlapping rate of ultrasonic trajectories is critical for suppressing damage during monocrystalline silicon grinding processes. As shown in Fig. 16, the material removal mechanisms under ultrasonic vibration are governed by two aspects: the internal factor involving microstructural evolution and the external factor related to stress field interactions. The continuous ultrasonic excitation promotes dislocation

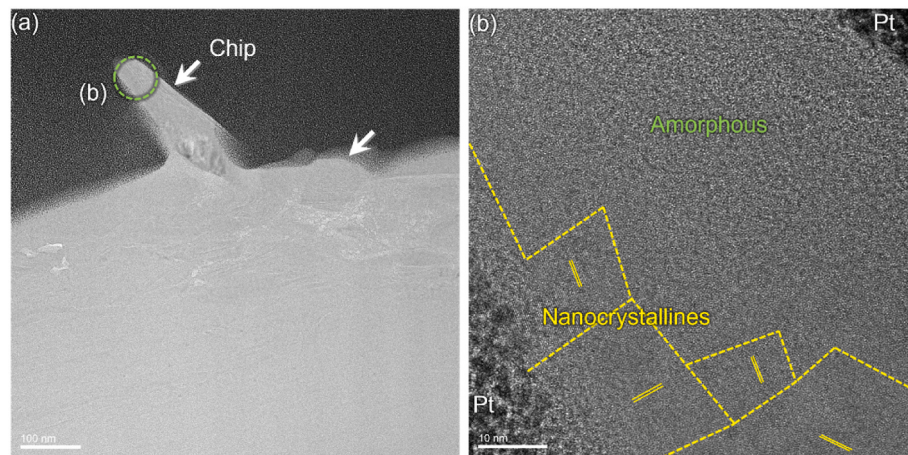


**Fig. 11.** (a) Bright-field images of powder-like chips, and (b) HRTEM image of the powder-like chips.

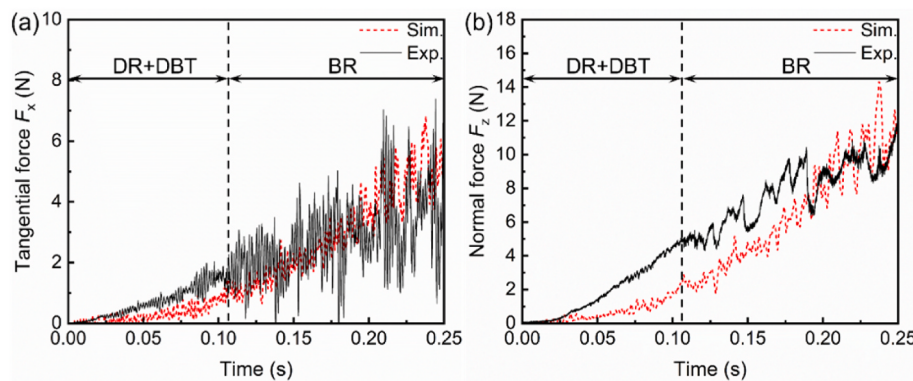


**Fig. 12.** Comparison of the scratching force between simulation and experiment: (a) Tangential force, and (b) Normal force.

motion and the amorphization of monocrystalline silicon from the high-pressure phase transition. The accumulation of microcracks from dislocation pile-up dissipates energy and relieves localized stress, preventing the formation of larger cracks and contributing to increased material brittleness. External factors mainly cover the superposition of high-frequency oscillatory stress waves and stress field offset, both of which have influences on the damage mechanisms and crack propagation directions. Enhanced interference of stress wave intensity at high overlapping rates induces lateral propagation of tensile stresses beneath the plastic zone, effectively constraining median crack propagation. Furthermore, the offset of the stress field is more pronounced for ultrasonic trajectories with low overlapping rates, resulting in severe edge cracks and conchoidal damage. In contrast, the stress field becomes relatively uniform for ultrasonic trajectories under higher overlapping rates, where smaller microcracks and minimal chipping along the scratch edges formed. The aforementioned microscopic morphology showed that the high overlapping rate of ultrasonic vibration suppressed crack propagation and effectively reduced localized damage on the monocrystalline silicon. Therefore, the high overlap degree of ultrasonic trajectories in UVAG is beneficial for achieving better surface integrity of monocrystalline silicon.

#### 4. Conclusions

In this work, to comprehensively understand the influences of ultrasonic vibration on the surface integrity of monocrystalline silicon in UVAS, the ultrasonic overlap effect and the ultrasonic motion trajectories on the potential damage inhibition mechanisms of monocrystalline silicon is undertaken. The main conclusions can be

summarized as follows:

- (1) The removed surface morphology of monocrystalline silicon undergoes evolution with ultrasonic overlapping rate. Under high overlapping rates, the surface morphology after diamond scratching of monocrystalline silicon involves ductile grooves and powder-like chips, with scratch edges remaining smooth and free from edge chipping.
- (2) Subsurface damages induced by high overlapping rates of scratching consist of amorphous layers, high-density dislocations, microcrack aggregation zones, and lateral crack propagation regions, while median cracks are notably absent. Powder-like chips exhibit polycrystalline and amorphous characteristics, originating from synergistic high-pressure phase transformation and cleavage fracture.
- (3) The increasing overlapping rates lead to shielding effects of lateral cracks by promoting superposition interference of stress waves beneath the plastic zone, effectively suppressing the propagation behavior of median cracks and consequently reducing subsurface damage depth in monocrystalline silicon.
- (4) The relatively slight offset in the stress field at the vibration angle of zero significantly shorten the length of lateral cracks, driving a morphological transition in edge damage from the macroscopic conchoidal chipping to the microcrack system. The synergistic interaction between ultrasonic stress wave interference and stress field weak offset remarkably enhance crack propagation resistance in hard and brittle materials.

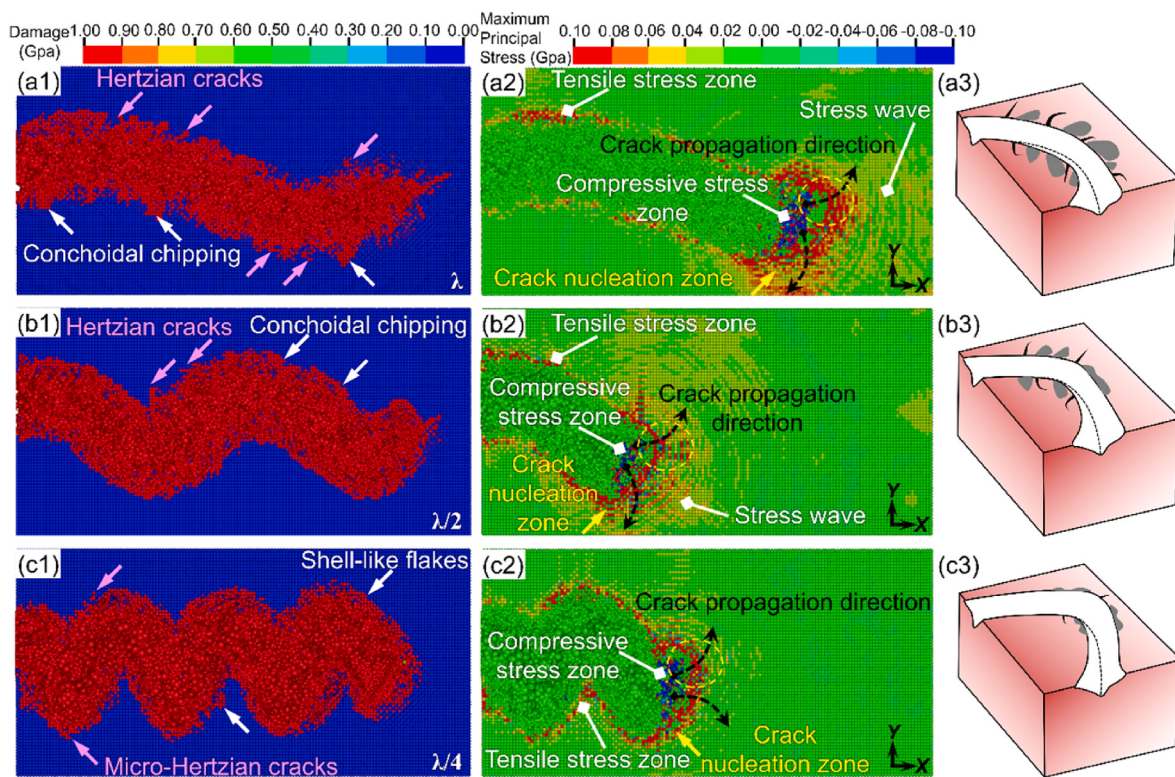


**Fig. 13.** Simulated damage distributions and stress fields of the scratching surface: (a) a wavelength of  $\lambda$ , (b) a wavelength of  $\lambda/2$ , and (c) a wavelength of  $\lambda/4$ .

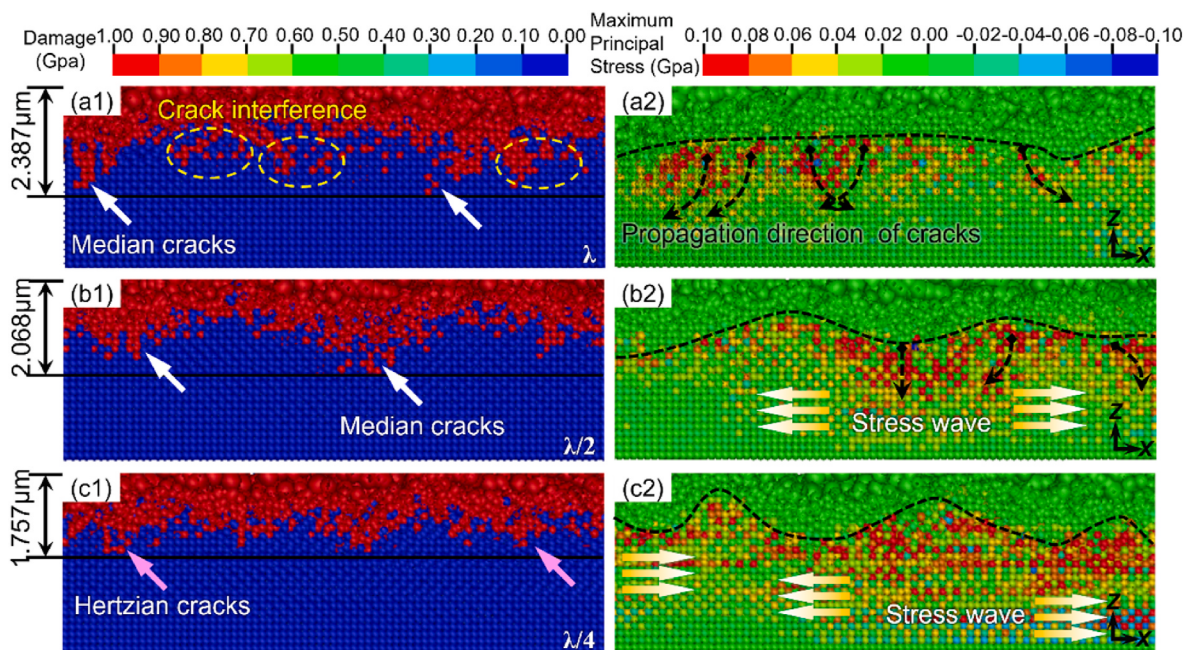


**Fig. 14.** Simulated subsurface damage distributions and stress fields of scratching: (a) a wavelength of  $\lambda$ , (b) a wavelength of  $\lambda/2$ , and (c) a wavelength of  $\lambda/4$ .

#### CRediT authorship contribution statement

**Jing Zhao:** Writing – original draft, Investigation. **Quanli Zhang:** Writing – review & editing, Methodology, Funding acquisition. **Yan Chen:** Supervision, Funding acquisition. **Yandan Zhu:** Resources, Investigation. **Chengqian Wang:** Funding acquisition, Conceptualization. **Zhimo Zhang:** Funding acquisition.

#### Declaration of competing interest

The authors declare that they have no known competing financial interests or personal relationships that could have appeared to influence the work reported in this paper.

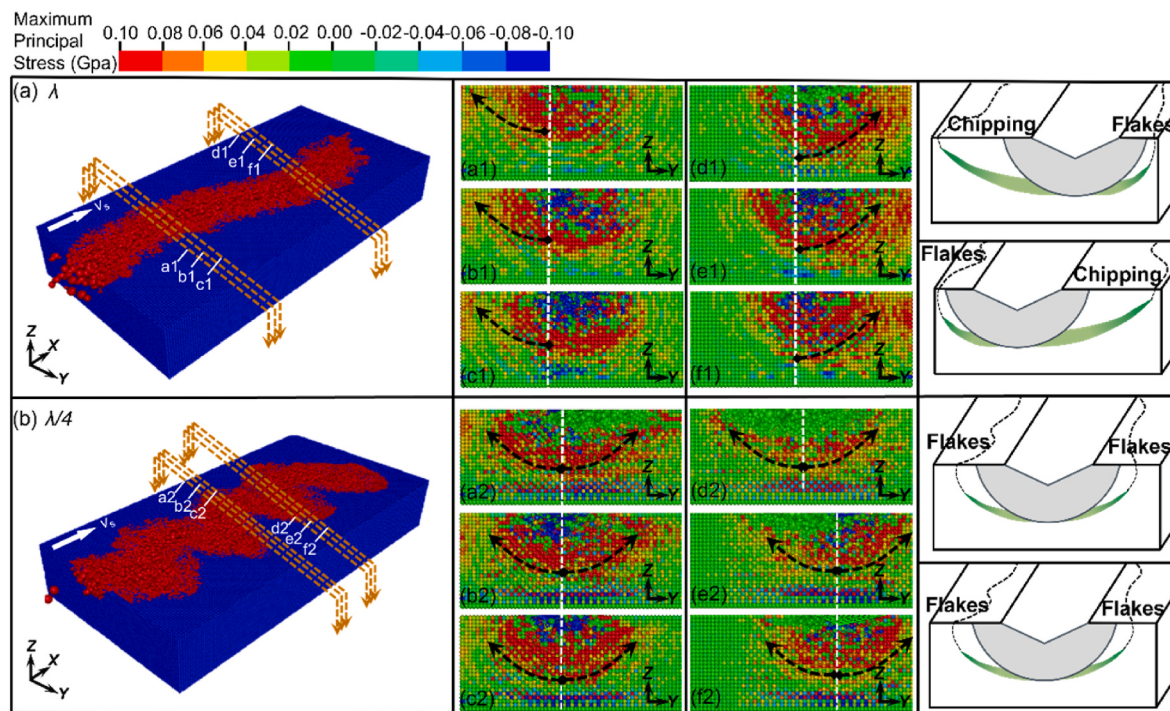


**Fig. 15.** Simulated instantaneous stress field of scratches at various overlapping rates: (a) a wavelength of  $\lambda$ , and (b) a wavelength of  $\lambda/4$ .

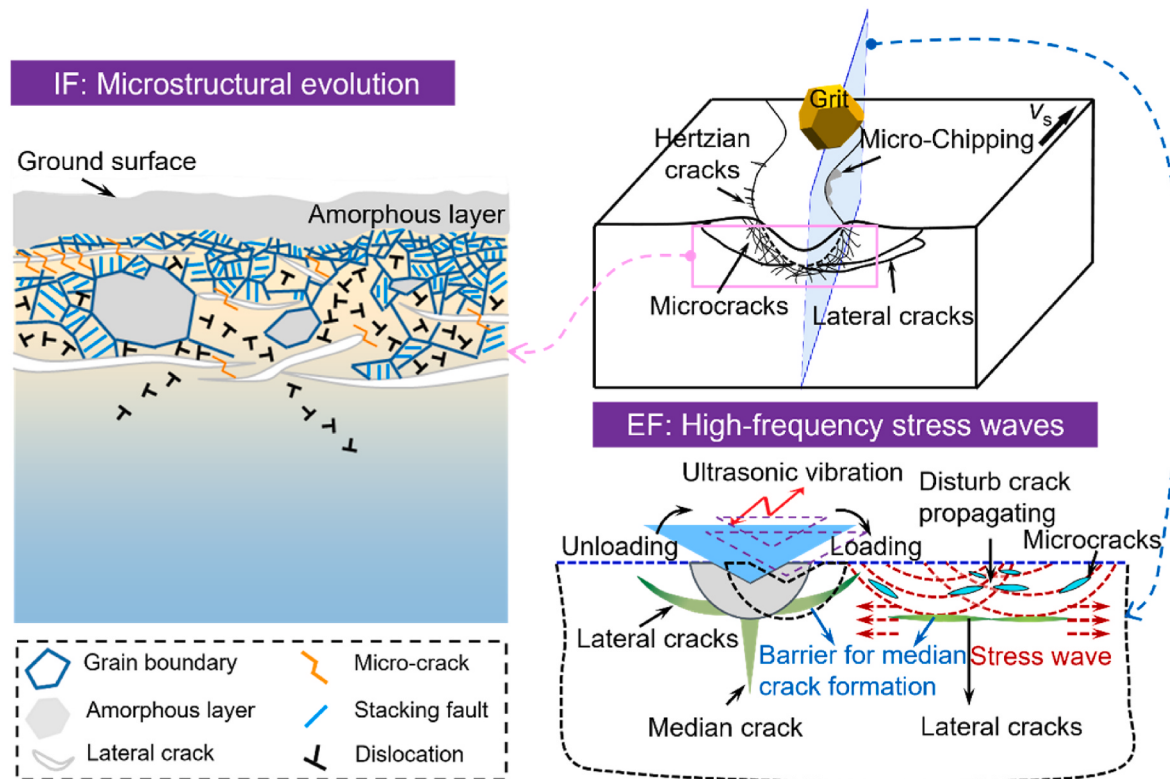


**Fig. 16.** Diagram of the damage mechanism of monocrystalline silicon in UVAS.

## Acknowledgments

The work was supported by the National Natural Science Foundation of China (NSFC) (No.: 52175412), the Open Fund of National Key Laboratory of Integrated Circuits and Microsystems (No.:

NICL2024KF2003) and National Key Laboratory of Science and Technology on Helicopter Transmission (No.: HTL-A-22G01).

## Data availability

Data will be made available on request.

## References

- [1] Z.J. Choong, D. Huo, P. Degenaar, A. O'Neill, Micro-machinability and edge chipping mechanism studies on diamond micro-milling of monocrystalline silicon, *J. Manuf. Process.* 38 (2019) 93–103.
- [2] Y. Kim, S. Jin, K. Park, J. Lee, J.-H. Lim, B. Yoo, Effect of pulse current and pre-annealing on thermal extrusion of Cu in through-silicon via (TSV), *Front. Chem.* 8 (2020).
- [3] H. Tao, Y. Liu, C. Wang, D. Zhao, X. Lu, Cutting speed dependence of material removal mechanism for monocrystal silicon, *Int. J. Mech. Sci.* 264 (2024) 108816.
- [4] S. James, S. Panchal, Finite element analysis and simulation study on micromachining of hybrid composite stacks using Micro Ultrasonic Machining process, *J. Manuf. Process.* 48 (2019) 283–296.
- [5] T. Gao, X. Zhang, C. Li, Y. Zhang, M. Yang, D. Jia, H. Ji, Y. Zhao, R. Li, P. Yao, L. Zhu, Surface morphology evaluation of multi-angle 2D ultrasonic vibration integrated with nanofluid minimum quantity lubrication grinding, *J. Manuf. Process.* 51 (2020) 44–61.
- [6] C. Huang, M. Zhou, H. Zhang, Investigations on the micro-interactions of grit-workpiece and forces prediction in ultrasonic vibration side grinding of optical glass, *J. Mater. Process. Technol.* 300 (2022) 117415.
- [7] J. Yin, Q. Bai, S. Goel, P. Zhou, B. Zhang, An analytical model to predict the depth of sub-surface damage for grinding of brittle materials, *CIRP J. Manuf. Sci. Technol.* 33 (2021) 454–464.
- [8] G. Sun, S. Wang, Q. Zhao, X. Ji, J. Ding, Material removal and surface generation mechanisms in rotary ultrasonic vibration-assisted aspheric grinding of glass ceramics, *Int. J. Adv. Manuf. Technol.* 130 (2024) 3721–3740.
- [9] Z. Wang, Y. Bao, K. Feng, B. Li, Z. Dong, R. Kang, Y. Wang, Characterization, quantitative evaluation, and formation mechanism of surface damage in ultrasonic vibration assisted scratching of Cr/SiC composites, *J. Eur. Ceram. Soc.* 44 (2024) 4502–4523.
- [10] Y. Huang, Y. Zhou, J. Li, F. Zhu, Materials removal mechanism and multi modes feature for silicon carbide during scratching, *Int. J. Mech. Sci.* 235 (2022) 107719.
- [11] X. Wang, Y. Ning, W. Zheng, X. Bao, Q. Zhao, S. Wang, Anisotropic mechanism of material removal and ductile-brittle transition in sapphire scratching based on acoustic emission signal, *J. Mater. Res. Technol.* 31 (2024) 2876–2899.
- [12] C. Li, Y. Piao, F. Zhang, Y. Zhang, Y. Hu, Y. Wang, Understand anisotropy dependence of damage evolution and material removal during nanoscratch of MgF<sub>2</sub> single crystals, *Int. J. Extrem. Manuf.* 5 (2023) 015101.
- [13] Z. Liang, X. Wang, Y. Wu, L. Xie, L. Jiao, W. Zhao, Experimental study on brittle–ductile transition in elliptical ultrasonic assisted grinding (EUAG) of monocrystal sapphire using single diamond abrasive grain, *Int. J. Mach. Tool Manufact.* 71 (2013) 41–51.
- [14] C. Zhang, P. Feng, J. Zhang, Ultrasonic vibration-assisted scratch-induced characteristics of C-plane sapphire with a spherical indenter, *Int. J. Mach. Tool Manufact.* 64 (2013) 38–48.
- [15] G. Sun, F. Shi, Q. Zhao, Z. Ma, D. Yang, Material removal behaviour in axial ultrasonic assisted scratching of Zerodur and ULE with a Vickers indenter, *Ceram. Int.* 46 (2020) 14613–14624.
- [16] G. Qiao, S. Yi, W. Zheng, M. Zhou, Material removal behavior and crack-inhibiting effect in ultrasonic vibration-assisted scratching of silicon nitride ceramics, *Ceram. Int.* 48 (2022) 4341–4351.
- [17] H. Liu, W. Xie, Y. Sun, X. Zhu, M. Wang, Investigations on brittle–ductile cutting transition and crack formation in diamond cutting of mono-crystalline silicon, *Int. J. Adv. Manuf. Technol.* 95 (2018) 317–326.
- [18] C. Liu, S. To, X. Sheng, J. Xu, Molecular dynamics simulation on crystal defects of single-crystal silicon during elliptical vibration cutting, *Int. J. Mech. Sci.* 244 (2023) 108072.
- [19] Z. Wang, D. Ma, T. Suo, Y. Li, A. Manes, Investigation into different numerical methods in predicting the response of aluminosilicate glass under quasi-static and impact loading conditions, *Int. J. Mech. Sci.* 196 (2021) 106286.
- [20] N. Duan, Y. Yu, W. Wang, X. Xu, SPH and FE coupled 3D simulation of monocrystal SiC scratching by single diamond grit, *Int. J. Refract. Metals Hard Mater.* 64 (2017) 279–293.
- [21] L. Li, P. Ge, Coupled SPH-FEM modeling of Berkovich indenter scratching of single-crystal silicon, *Mater. Sci. Semicond. Process.* 173 (2024) 108155.
- [22] B. Lin, S. Li, Z.C. Cao, Y. Zhang, X.M. Jiang, Theoretical modeling and experimental analysis of single-grain scratching mechanism of fused quartz glass, *J. Mater. Process. Technol.* 293 (2021) 117090.
- [23] M. Li, X. Guo, S. Dai, S. Yuan, J. Ma, F. Liu, L. Zhang, D. Guo, P. Zhou, Effect of grinding damage on cutting force and ductile machining during single grain scratching of monocrystalline silicon, *Mater. Sci. Semicond. Process.* 151 (2022) 107019.
- [24] R.A. Gingold, J.J. Monaghan, Smoothed particle hydrodynamics: theory and application to non-spherical stars, *Mon. Not. Roy. Astron. Soc.* 3 (1977) 375–389.
- [25] G.R. Johnson, T.J. Holmquist, An improved computational constitutive model for brittle materials, in: AIP Conference Proceedings, AIP, Colorado Springs, Colorado (USA), 1994, pp. 981–984.
- [26] B. Wang, S.N. Melkote, P. Wang, S. Saraogi, Effect of speed on material removal behavior in scribing of monocrystalline silicon, *Precis. Eng.* 66 (2020) 315–323.
- [27] Y. Zhang, S. Zhu, Y. Zhao, Y. Yin, A material point method based investigation on crack classification and transformation induced by grit geometry during scratching silicon carbide, *Int. J. Mach. Tool Manufact.* 177 (2022) 103884.
- [28] Z. Li, S. Yuan, J. Ma, J. Shen, A.D.L. Batako, Study on the surface formation mechanism in scratching test with different ultrasonic vibration forms, *J. Mater. Process. Technol.* 294 (2021) 117108.
- [29] R.J. Stokes, T.L. Johnston, C.H. Li, Crack formation in magnesium oxide single crystals, *Philos. Mag.* 3 (1958) 718–725.
- [30] C. Li, F. Zhang, Y. Wu, X. Zhang, Influence of strain rate effect on material removal and deformation mechanism based on ductile nanoscratch tests of Lu2O3 single crystal, *Ceram. Int.* 44 (2018) 21486–21498.
- [31] Z. Wang, J. Chen, G. Wang, Q. Bai, Y. Liang, Anisotropy of single-crystal silicon in nanometric cutting, *Nanoscale Res. Lett.* 12 (2017).
- [32] F. Zhao, B. Lin, Y. He, T. Sui, H. Li, P. Zhao, Curvature effect induced cutting stress field offset and its influence on the damage of hard and brittle materials, *J. Mater. Process. Technol.* 303 (2022) 117526.